SCIENTIFIC REPORTS

OPEN

Superconductivity Series in Transition Metal Dichalcogenides by Ionic Gating

Received: 12 February 2015
Accepted: 02 July 2015
Published: 03 August 2015

Wu Shi[1], Jianting Ye[1,2], Yijin Zhang[1], Ryuji Suzuki[1], Masaro Yoshida[1], Jun Miyazaki[1], Naoko Inoue[1], Yu Saito[1] & Yoshihiro Iwasa[1,3]

Functionalities of two-dimensional (2D) crystals based on semiconducting transition metal dichalcogenides (TMDs) have now stemmed from simple field effect transistors (FETs) to a variety of electronic and opto-valleytronic devices, and even to superconductivity. Among them, superconductivity is the least studied property in TMDs due to methodological difficulty accessing it in different TMD species. Here, we report the systematic study of superconductivity in $MoSe_2$, $MoTe_2$ and WS_2 by ionic gating in different regimes. Electrostatic gating using ionic liquid was able to induce superconductivity in $MoSe_2$ but not in $MoTe_2$ because of inefficient electron accumulation limited by electronic band alignment. Alternative gating using $KClO_4$/polyethylene glycol enabled a crossover from surface doping to bulk doping, which induced superconductivities in $MoTe_2$ and WS_2 electrochemically. These new varieties greatly enriched the TMD superconductor families and unveiled critical methodology to expand the capability of ionic gating to other materials.

Semiconducting transition metal dichalcogenides (TMDs) have attracted considerable interest as typical two-dimensional (2D) materials. Atomically flat and chemically stable thin layers of TMDs can be readily obtained via graphene-like mechanical exfoliation[1] from bulk crystals due to the weak van der Waals interaction-based interlayer bonding[2]. By virtue of their semiconducting nature and defect-free crystal surfaces, thin exfoliated TMD layers are regarded to be ideal channel materials for field-effect transistors (FETs)[3–5] and TMD-based FETs have been shown to possess remarkable electronic[6,7] and opto-valleytronic properties[8–13] as well as promising prospects for device applications[14].

Recent advances in the application of the field effect have been achieved using ionic gating by the formation of electrical double layers (EDLs); an EDL consists of narrow (~1 nm) spatial charge doublets that mimic a capacitor capable of accumulating an ultra-dense sheet of carriers (~10^{14} cm^{-2})[15]. EDL transistors (EDLTs) based on electrostatic ionic gating have proven to be a versatile tool for achieving novel device functionalities[16,17] and inducing new electronic states[18–21] at the interface between an ionic medium and a semiconductor channel. The use of EDLTs in TMD research has enabled the investigation of various interesting electronic properties, including ambipolar transport[3,5], electric field control of spin polarization[22], and circularly polarized electroluminescence[12]. High-density carriers have also bridged the gap to the quantum phases of TMDs through the field effect. The discovery of gate-induced superconductivity in MoS_2 has revealed enhanced T_c and a dome-like phase diagram[23]; these features are absent in the chemically doped phase. In light of other available semiconducting TMDs and the effectiveness of electrostatic ionic gating, it is anticipated that this method may be applicable to induce superconductivity in other TMDs.

[1]Quantum-Phase Electronics Center and Department of Applied Physics, The University of Tokyo, 7-3-1 Hongo, Bunkyo-ku, Tokyo, 113-8656, Japan. [2]Zernike Institute for Advanced Materials, University of Groningen, The Netherlands. [3]Center for Emergent Matter Science, RIKEN, Hirosawa 2-1, Wako 351-0198, Japan. Correspondence and requests for materials should be addressed to W.S. (email: shiwu@ap.t.u-tokyo.ac.jp) or Y.I. (email: iwasa@ap.t.u-tokyo.ac.jp)

Following the previous work on MoS_2[5,23], here, we report a comprehensive study of transport properties and superconductivity in a semiconducting TMD series, specifically 2*H*-type $MoSe_2$, $MoTe_2$ and WS_2. Transistor operation and carrier accumulation were significantly influenced by the interfacial energy level alignments of the different TMD materials at the same electrostatic ionic gating using an ionic liquid (IL: DEME-TFSI). Subsequently, the TMDs showed similar gate-induced insulator–metal transitions but did not all reach the superconducting states. In $MoSe_2$, new gate-induced superconductivity (GIS) was found with a maximum T_c of 7.1 K that follows a dome-shaped phase diagram similar to that of MoS_2[20,23]. However, no superconductivity was observed in $MoTe_2$ because of the low efficiency of electrostatic electron accumulation that could be achieved in this material using an IL. When the IL was replaced with a $KClO_4$/PEG electrolyte, the electron doping could be significantly enhanced through a crossover to an electrochemical regime beyond the electrostatic limit. As a result, superconductivity in 2*H*-$MoTe_2$ and WS_2 were enabled with observed T_c values of approximately 2.8 K and 8.6 K, respectively. Thus, these results have revealed two series of superconductors in these TMDs. Additionally, this study established new strategies for ionic gating both for electrostatic charge accumulation and electrochemical carrier doping, thereby providing new capability for accessing a wide carrier concentration range and extending superconductivity in other material series.

Results

Evolution of electrostatic charge accumulation in MoX_2 EDLTs. Figure 1a illustrates the crystal structure of 2*H*-type transition metal dichalcogenides, MX_2 (M = Mo or W; X = S, Se or Te), consisting of two-dimensional covalently bonded X−M−X layers. Due to their weak bonds formed through van der Waals interactions between the layers, thin flakes of MX_2 can be readily isolated from bulk material via mechanical exfoliation and then fabricated into FET devices (see the Methods section). We used the EDLT structure and employed DEME-TFSI as a gate dielectric; the latter is a widely used IL that has been demonstrated to be capable of accumulating a high density of carriers at the interface even at low bias voltages[15]. Figure 1b presents a schematic diagram of the EDLT configuration and an optical image (bottom left) of a real MX_2 device ($MoSe_2$) prior to the application of the IL. A typical Hall bar geometry was adopted to measure the four-terminal resistance and the Hall carrier density. The thickness of the MoX_2 flakes in this work ranged from approximately 20 nm to 100 nm as measured by atomic force microscopy (AFM). We confirmed that the 2*H*-type crystal structure was maintained in the thin flakes after transport measurements with IL gating as confirmed by synchrotron microbeam X-ray diffraction experiments (see Fig. S1 and Table S1 in the Supplementary Information).

The gate voltage was applied through a droplet of IL under high vacuum and at a temperature just above the glass transition temperature of DEME-TFSI (i.e., 220 K) to suppress potential chemical reactions between the IL and the film surface[5]. Under these conditions, a TMD thin-flake EDLT can be modeled as a simple contact heterostructure between a semiconductor (i.e., the molybdenum-based TMD) and an electrolyte (i.e., the IL). Following the terminology used for electrolyte/semiconductor interface[24–27], Fig. 1c,d present schematic energy-level diagrams before and after making the IL/TMD interface. Here, TMD refers specifically to a 2*H*-type MX_2 with a finite band gap[28,29]. Even before applying a gate voltage, the electric double layer is formed and, in some cases, charge transfer across the interface (electrolysis) takes place until equilibrium is reached, i.e., the redox potential of the electrolyte (E_{redox}) aligns with the Fermi energy of the semiconductor (E_F)[24–27]. The space charge layer in the semiconductor has an associated electric field represented by band bending. The work function Φ_{TMD} influences the initial charge redistribution and the band bending at the interface before application of gate voltage. Because TMD work functions differ from each other[30], the initial band bending varies among MoS_2, $MoSe_2$ and $MoTe_2$ thin flakes for the same IL. Among these three dichalcogenides, $MoTe_2$ exhibits the smallest work function, leading to the weakest initial band bending and the largest carrier injection barrier for electrons. Therefore, a systematic evolution of transistor performance with increasing threshold voltage is expected when the channel material is changed from MoS_2 to $MoTe_2$.

By sweeping the gate voltages at a constant rate of 20 mV/s at 220 K, we measured the transfer curves for the different MoX_2 (21 devices in total) that were all gated using DEME-TFSI. Figure 2a presents a comparison of the typical transfer curves of MoS_2, $MoSe_2$ and $MoTe_2$ EDLTs measured with $V_{DS} = 0.1$ V. All three MoX_2 transistors displayed ambipolar behavior with systematic properties: within the same bias range, the two extremes of preferences for electron and hole accumulation were dominated by MoS_2 and $MoTe_2$, respectively, whereas $MoSe_2$ exhibited a well-balanced ambipolar transistor performance that was most suitable for light-emitting devices[31]. The electron and hole conduction threshold voltages (as indicated by the black dashed lines in Fig. 2a) progressively shifted to higher voltages from MoS_2 to $MoTe_2$. The average values of the threshold voltage V_{th} versus the MoX_2 work function (from ref. 30) are plotted in Fig. 2b, with each data point obtained by averaging 7 devices and the standard deviations shown by the error bars. The electron and hole conduction V_{th} values decreased with increasing MoX_2 work function, consistent with the discussion of the interfacial energy-level alignment presented above. It is well known that in conventional FETs, V_{th} is largely governed by the contact effects (work function mismatch between the contact and the semiconductor) and by the deep trap states in the energy gap. However, it is noted that both of these factors take only minor roles in EDLTs[5,32]. First, the electrostatic screening (due to the ions close to the metal contact/semiconductor interface) in the liquid can further reduce the width of the Schottky barrier down to values comparable to the electrostatic screening

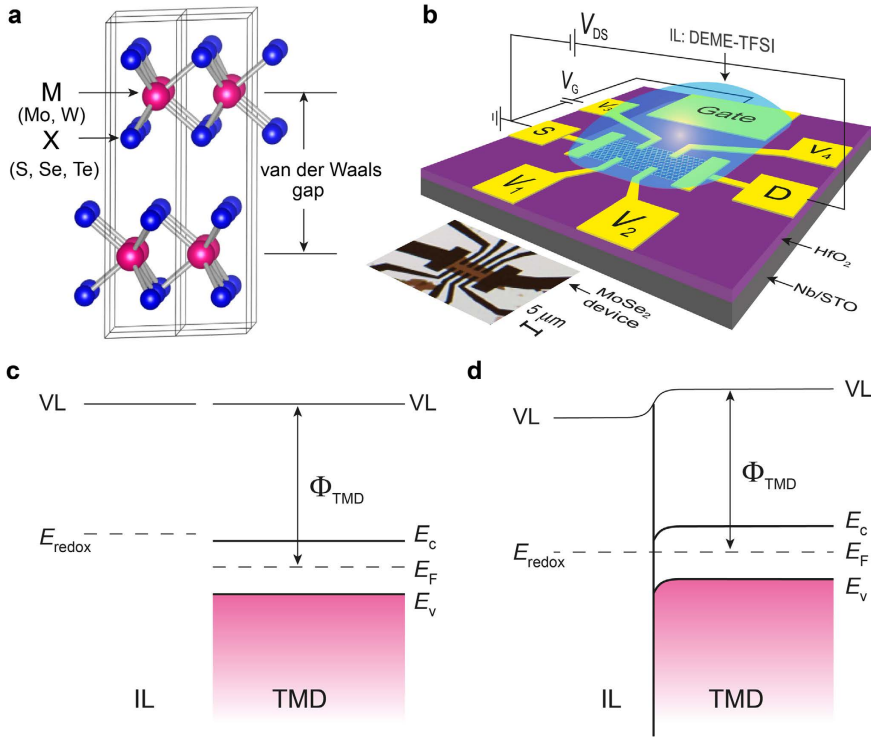

Figure 1. Transition metal dichalcogenide (TMD) EDLT device and schematic diagrams of energy-level alignment at the IL/TMD interface. (**a**) Crystal structure of a 2*H*-type layered transition metal dichalcogenide MX_2; M = Mo or W and X = S, Se, or Te. (**b**) EDLT device and measurement configuration. The bottom left shows an actual $MoSe_2$ nanoflake device with a Hall bar geometry. This figure is drawn by W.S. (**c**) Schematic diagram of the energy levels of an independent ionic liquid and a TMD. (**d**) Schematic diagram of aligned energy levels at the IL/TMD interface. The initial band bending occurs when the IL touches the TMD surface. The vacuum level (VL), redox potential (E_{redox}), conduction band (E_c), valence band (E_v), Fermi energy (E_F), and work function (Φ_{TMD}) are defined and labeled in (**c**) and (**d**).

length in the ionic liquid (1–2 nm)[5,32–34]. Thus, tunneling-mediated carrier injection is more likely than thermal activation over a Schottky barrier. Second, because of the extremely large EDL capacitance C_{EDL} (usually two orders of magnitude larger than the solid gate capacitance C_{solid}), the threshold voltage shift ΔV_{th} ($=N_{trap}/eC_{EDL}$) due to the filling of trap states (N_{trap}) becomes negligible[32].

Because our devices were designed to access low-temperature quantum phases, it was critical to quantify the sheet carrier density n_{2D}, which was therefore unambiguously determined through a Hall effect measurement. To eliminate any temporal change in n_{2D} during ionic gating in MoX_2 EDLTs, all Hall effect measurements were performed at temperatures below the freezing point of ion movement, where the total number of accumulated carriers is fixed. The Hall coefficient R_H was found to change its sign as a function of the gate voltage V_G and $n_{2D} = 1/|R_H e|$ was linearly proportional to the gate bias V_G in the electrostatic region (Fig. S2). The EDL capacitance can be derived through a linear fit to the n_{2D}–V_G plot. We focused on the electron side and compared the capacitances obtained from the n_{2D}–V_G plots for 15 different MoX_2 devices, as shown in Fig. 2c. Even for the same MoX_2 crystal and IL, the capacitance values were broadly distributed among the devices, possibly because of the existence of different surface states in the individual thin flakes after the fabrication process. However, $MoTe_2$ clearly exhibited a smaller average capacitance value (4.1 μF/cm^2) than MoS_2 (8.6 μF/cm^2) or $MoSe_2$ (10.6 μF/cm^2), indicating that $MoTe_2$ demonstrated the lowest efficiency in electron accumulation.

Superconductivity of $MoSe_2$ by ionic liquid gating in an electrostatic regime. To verify that the electrostatic ionic gating method[23] described above is applicable for inducing superconductivity in $MoSe_2$ and $MoTe_2$ thin flake EDLTs, we measured their transport properties down to 2 K by varying V_G in the positive direction to access electron transport. The results are shown in the plot of the channel sheet resistance R_s versus T in Fig. S3 and the $MoSe_2$ data are presented in Fig. 3a. All materials displayed clear insulator–metal transitions with increasing electron density under higher V_G (Fig. S3). As shown in Fig. 3a, gate-induced superconductivity emerged in $MoSe_2$ at $V_G = 2.4$ V and developed further with further V_G increase. However, no superconducting transition was observed in $MoTe_2$ up to $V_G = 2.5$ V (Fig. S3c), at which point a conductivity maximum was reached. At higher V_G values, the carrier density

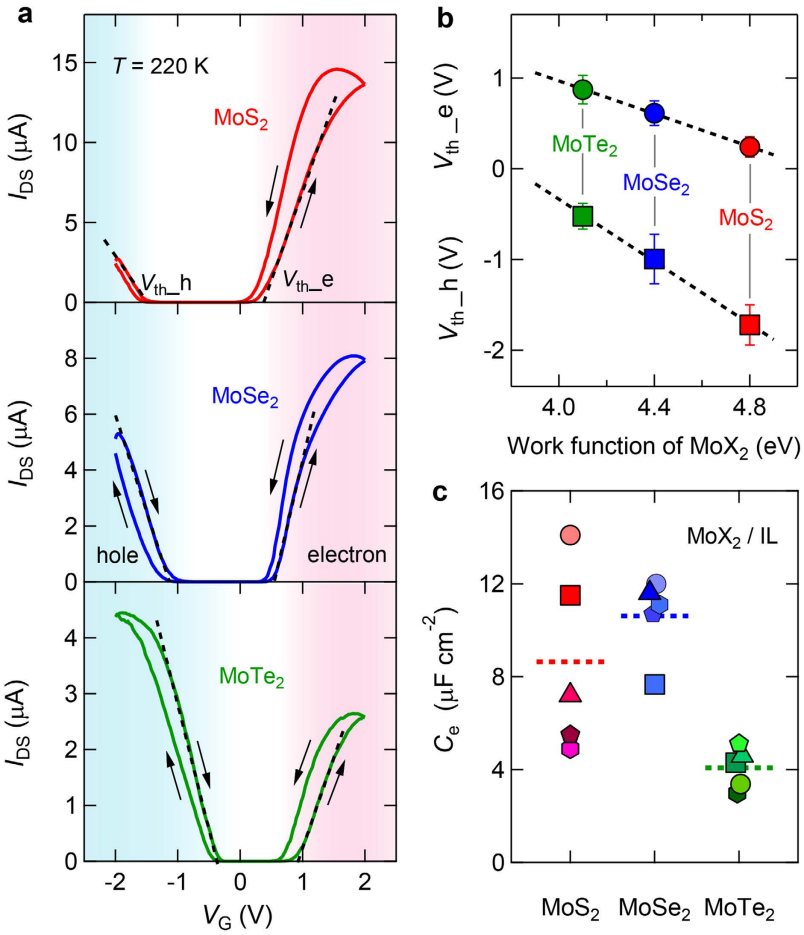

Figure 2. Evolution of ambipolar transfer characteristics and electrostatic charge accumulation in MoX_2 EDLTs. (**a**) Comparison of typical ambipolar transfer curves of MoS_2, $MoSe_2$ and $MoTe_2$ EDLTs measured with $V_{DS} = 0.1$ V at 220 K. V_G was swept at a constant rate of 20 mV/s through the same IL, DEME-TFSI. The threshold voltages for the electron side (V_{th}_e) and the hole side (V_{th}_h) were determined by linearly extrapolating the I_{DS}–V_G curves to zero, as indicated by the black dashed lines. (**b**) Linear correlation between the threshold voltages and the work functions of MoX_2. The threshold voltages are average values deduced from the transfer curves of 21 MoX_2 devices with the same IL at 220 K. According to the black dashed lines, a semiconductor with a smaller work function exhibits larger or smaller threshold voltages for electron or hole accumulation, respectively. This can be explained by considering the energy-level alignment at the interface, as shown in Fig. 1d. (**c**) Capacitances for electron accumulation, C_e, deduced from sheet carrier density n_{2D}–V_G plots (Fig. S2b) for various MoX_2 EDLT devices using the same IL, DEME-TFSI. Different symbols represent different devices, and the horizontal short dashed lines correspond to the average values. On average, $MoTe_2$ exhibited the lowest EDL capacitance for electron accumulation.

was saturated (Fig. S6b) and the mobility decreased, precluding the formation of a more pronounced conducting state. The transport measurements were also conducted for all MoX_2 devices via hole doping. Similar insulator–metal transitions also occurred as negative V_G was applied (Fig. S4), but no hole superconductivity was observed down to 2 K for all MoX_2. Further enhancement of hole density or decrease in temperature is required to achieve hole superconductivity.

Now we consider the properties of the electron-doped superconductor. Figure 3b presents the temperature dependence of the normalized sheet resistance of the $MoSe_2$ device at various V_G (i.e., the device represented in Fig. 3a). It is evident that the superconducting transition can be controlled via electrostatic ionic gating. The T_c value increased with increasing V_G, reaching a maximum of $T_c = 7.1$ K (defined as 90% of the total transition at $V_G = 3.2$ V, where $n_{2D} = 1.69 \times 10^{14}$ cm^{-2}). This T_c value was higher than the maximum previously reported for Sr-doped $MoSe_2$ (~5 K)[35]. Based on a precise determination of n_{2D} using the Hall effect (Fig. S2), we show the relationship between T_c and n_{2D} for the same $MoSe_2$ device in Fig. 3c. In a similar manner to MoS_2, the superconductivity in $MoSe_2$ abruptly emerged above a critical carrier density n_0. Subsequently, T_c increased with increasing n_{2D} until a maximum was reached. This trend was also consistently observed in the H_{c2} versus n_{2D} phase diagram (Fig. S5). These similarities

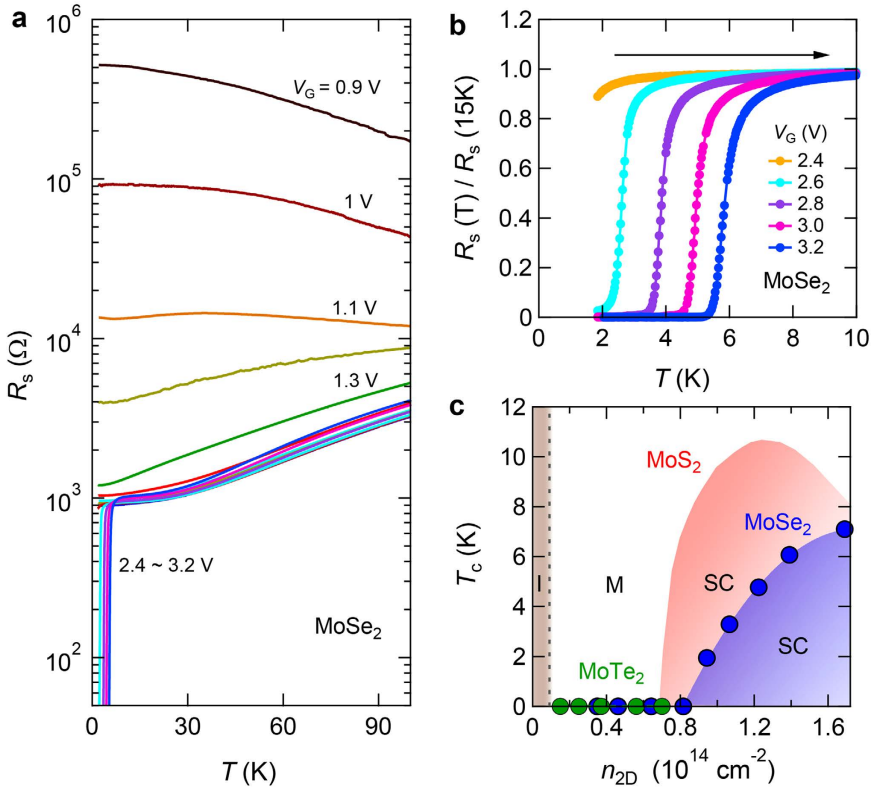

Figure 3. Superconductivity induced by electrostatic IL gating and phase diagram of electron-doped $MoSe_2$. (**a**) Temperature dependence of the channel sheet resistance R_s at various liquid gate voltages for a $MoSe_2$ EDLT device using DEME-TFSI as ionic media. (**b**) Normalized channel sheet resistance R_s/R_s (15 K) of the same $MoSe_2$ EDLT device as a function of temperature for various liquid gate voltages from 2.4 V to 3.2 V. (**c**) T_c versus n_{2D} phase diagram of electron-doped $MoSe_2$. The MoS_2 phase diagram (red shade) was taken from ref. 23 for comparison. Here, sheet carrier density n_{2D} is obtained from Hall effect measurements and T_c is defined as the position corresponding to 90% of the total resistance drop. $MoTe_2$ data are also presented in (**c**), showing no evidence of superconductivity down to 2 K ($T_c = 0$) because of the insufficient maximum carrier density achieved through electrostatic IL gating.

in the behaviors of MoS_2 (red shade in Fig. 3c) and $MoSe_2$ thus indicated that the dome-shaped phase diagram is a universal feature of gate-induced superconductivity in TMD systems. Figure 3c also shows n_{2D} values for multiple $MoTe_2$ devices (denoted by green symbols) with $T_c = 0$, indicating that no superconducting transitions were observed down to 2 K. We believe that the absence of superconductivity in $MoTe_2$ may be due to the low maximum n_{2D} of approximately 0.7×10^{14} cm^{-2}, which is much smaller than the accumulation on MoS_2 or $MoSe_2$. This difference can be attributed to the fact that $MoTe_2$ demonstrated the largest threshold voltage V_{th} (bottom panel of Fig. 2a) and the smallest capacitance C_e (Fig. 2c) during transistor operation in the electrostatic region.

Superconductivity of $MoTe_2$ by electrolyte gating in an intermediate doping regime. To induce superconductivity in $MoTe_2$, it is necessary to enhance the carrier density through more efficient transistor operation. The threshold voltage can be reduced by choosing ILs with smaller work functions. However, this achieved only a moderate enhancement in the carrier density because of the slight increase in capacitance and a significant n_{2D} saturation observed with increasing V_G (Fig. S6). We then found that the limitations on carrier accumulation could be surmounted by replacing the organic IL with the $KClO_4$/PEG electrolyte. Figure 4a compares the channel current values I_{DS} for $MoTe_2$ devices fabricated using the two ionic media: the IL (DEME-TFSI) and the $KClO_4$/PEG electrolyte. For IL gating, an increase in I_{DS} was initiated at a large threshold voltage of approximately 1 V and was no longer observed when V_G exceeded 2.5 V, indicating a limit on the formation of a more conductive channel. This peak behavior of I_{DS} versus V_G was associated with n_{2D} saturation and was confirmed in multiple devices, implying that the observed behavior was not related to device degradation. For $KClO_4$/PEG electrolyte gating, electrostatic electron accumulation occurred at a much smaller threshold voltage and induced a rapid increase of I_{DS}, reaching a high conducting state at V_G approximately 3.5 V. The conducting state was then sustained as V_G was continuously increased up to 6 V. This gave rise to the observation of good metallic conduction followed by a superconducting transition at low temperatures, as shown in Fig. 4b.

The magnetic field dependence of the R_s-T curves (Fig. 4c) further confirmed the existence of superconductivity at $T_c = 2.8$ K (defined as the temperature corresponding to 90% of the normal-state resistance at $H = 1$ T). Since superconductivity in $MoTe_2$ has never been reported, the result in Fig. 4 marks the discovery of a new superconductor in the 2*H*-MoX_2 family.

Limited by the much lower ionic mobility in an electrolyte compared with an IL, we applied a V_G at 300 K for the $KClO_4$/PEG electrolyte; at this temperature, the ions were sufficiently mobile. At such a high temperature, an increase in the leakage current associated with the saturation of I_{DS} was observed above $V_G = 3.5$ V (as shown in the inset of Fig. 4a), indicating that electrolysis of PEG or potassium intercalation may have occurred. At 20 K, n_{2D} reached 0.9×10^{14} cm^{-2}, only slightly higher than the maximum observed for IL gating. We define this voltage range for nearly saturated I_{DS} as an intermediate regime beyond the electrostatic limit as it could be followed by an electrochemical regime at a higher V_G where potassium intercalation may occur more effectively into the entire flake and eventually become dominant.

Superconductivity of WS_2 by electrolyte gating in an electrochemical regime. WS_2 is another member of semiconducting TMDs, where bulk superconductivity was known to occur at 3.5 K by conventional chemical doping of Sr[35]. Recently, ionic gating using IL was found to induce superconductivity at 4 K[36]. To confirm the different doping mechanism using the $KClO_4$/PEG electrolyte as ionic media and gain access deeper into the electrochemical regime in WS_2, we further increased our voltage bias up to 12 V and systematically studied the evolution of carrier accumulation in a WS_2 device labeled as A. Figure 5a presents the channel current values I_{DS} as a function of V_G measured at 300 K (see the complete data in Fig. S7). We can see that I_{DS} went through the similar electrostatic and intermediate doping regimes reaching a limited value similar to that of $MoTe_2$ described above; however, here, the limited I_{DS} (approximately 17 μA at $V_G = 6$ V) corresponded to a metallic state that failed to access the superconducting region. This limit was clearly broken when V_G exceeded approximately 7 V, where a second rapid upturn of I_{DS} strongly indicated an effective electrochemical doping process, *i.e.*, ion intercalation under high bias. This was supported by the distinctive large hysteresis (magenta dashed line in Fig. 5a) manifesting the intercalation and de-intercalation in a V_G scan cycle. Because the device nearly recovered its pristine state after V_G was restored back to zero, the low temperature transport can be measured after the *in situ* change of V_G in a similar way as for the measurements in the electrostatic regime using ionic liquids. As shown in Fig. 5a, we also measured the carrier density n_{Hall} by the Hall effect at 200 K (also see Fig. S8). Here, n_{Hall} corresponds to the sheet carrier density n_{2D} in the electrostatic regime, whereas beyond the electrostatic regime, n_{Hall} corresponds to the projected carrier density, which is essentially the bulk density n_{3D} multiplied by the thickness of the doped sample. Examination of the n_{2D} values (as shown in Fig. 5a) measured by the Hall effect at 200 K (denoted by circle symbols) showed that in the intermediate region, n_{Hall} increased very slowly until reaching an upper limit V_G of approximately 7 V; this is followed by a rapid n_{Hall} increase reaching $n_{Hall} = 4.7 \times 10^{15}$ cm^{-2} at $V_G = 12$ V, more than one order of magnitude higher than the maximum value obtained in the electrostatic region. Accordingly, the capacitance deduced from the $n_{Hall}-V_G$ data in the electrochemical region was much higher, achieving up to 200 μF/cm^2, providing strong evidence that the carrier doping reaches far beyond the level achieved in the electrostatic regime.

We then focused on the transport properties of the electrochemically doped WS_2. Figure 5b presents the results for R_S as a function of temperature on the log scale for device A at various V_G from 6 V to 12 V. We observed good metallic conduction followed by a superconducting transition at the same onset transition temperature (the dashed vertical line in Fig. 5b) for V_G at 9 V, 10 V and 12 V. The transition can be completely destroyed by applying a magnetic field of 2 T as indicated by the dashed curves in Fig. 5b, providing strong evidence of superconductivity. Unlike the gate modulation of T_c observed in IL-gated $MoSe_2$ (Fig. 3b), here, the onset T_c value did not change with V_G. One possible explanation is that the superconducting phase is a line-phase compound in terms of K concentration. Potassium ions started to intercalate between the WS_2 layers when V_G exceeded a critical value (~7 V for device A). Then, a particular K_xWS_2 line-phase compound that exhibited a superconducting transition with a fixed T_c was formed at approximately 9 V. In this initial state where superconductivity appeared, the sample consists of a mixture of nonsuperconducting phase with lower x and the superconducting phase. As V_G further increased, the superconducting phase gradually grew and finally occupied a substantial portion of the whole channel, reaching the "zero resistance" state ($R_s < 0.02$ Ω, limited by our measurement resolution). This is also supported by the gradual decrease of the normal state resistance with increasing V_G (Fig. 5b).

Similar superconducting transitions were also observed in other devices. The inset in Fig. 5b presents R_s versus T curves in the same log scale for another WS_2 sample (device B). Superconducting transitions were well developed down to "zero resistance" for $V_G = 8$ V. When intercalation further proceeded, an overdoped phase started to grow, forming a mixture of the superconducting phase and the overdoped non-superconducting phase. Finally, zero-resistance disappeared since an overdoped metallic state became dominant at $V_G = 10$ V, where a high n_{Hall} of approximately 2.1×10^{16} cm^{-2} was achieved. With the ability of reaching such a high carrier density, this gate-controllable intercalation process is also applicable to metallic TMD system[37]. The critical V_G varies from sample to sample due to the differences in sample thicknesses and device configurations even following the same gating procedure. Here, n_{Hall} is

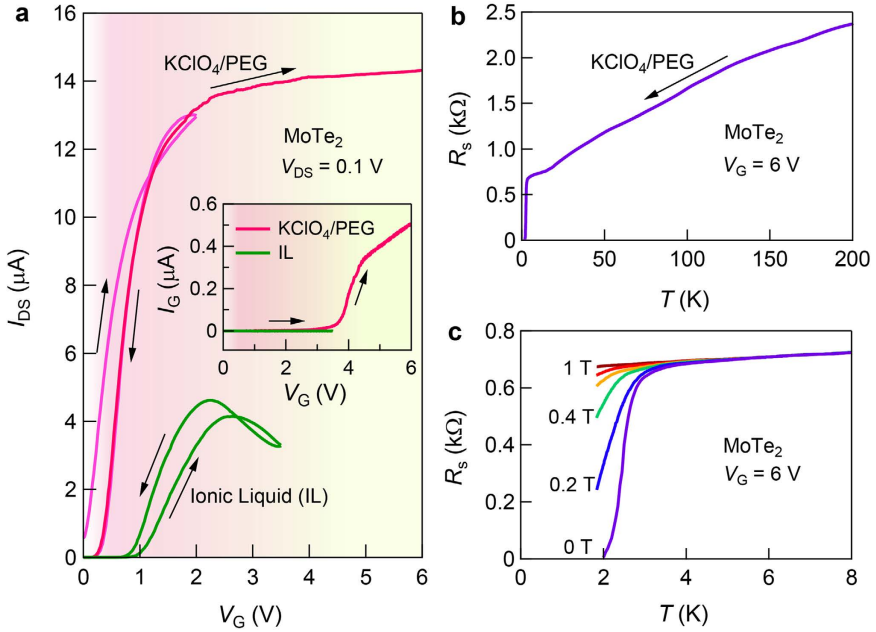

Figure 4. Transistor operation characteristics, I_{DS}–V_G and superconductivity in electron-doped $MoTe_2$ with $KClO_4$/PEG as ionic media. (**a**) Comparison of the transfer curves of 2*H*-$MoTe_2$ devices obtained by sweeping the IL gate at 220 K and the $KClO_4$/PEG gate at 300 K at constant rate of 20 mV/s with $V_{DS} = 0.1$ V. The inset presents a comparison of the leakage current I_G as a function of the gate voltage. A reduction in V_{th}_e and a significant enhancement of the ON-state current was observed with the $KClO_4$/PEG gate. (**b**) Channel sheet resistance R_s of the same 2*H*-$MoTe_2$ device with the $KClO_4$/PEG gate at $V_G = 6$ V as a function of temperature. (**c**) Temperature dependence of R_s for various magnetic fields from 0 T to 1 T. The superconducting transition temperature T_c, defined as the temperature corresponding to 90% of the normal-state resistance at 1 T, is 2.8 K at $V_G = 6$ V.

important to quantify the doping level of the flake. Assuming that the whole flake was uniformly doped, the bulk carrier density n_{3D} and the doping concentration x can be deduced from the Hall effect and the thickness of the thin flake. Figure 5c shows the phase diagram for T_c versus n_{3D} (bottom horizontal axis) and doping concentration x (upper horizontal axis) collected from four different devices with superconducting transitions reaching "zero resistance", where T_c was defined as the temperature corresponding to 90% of the total transition. The similar T_c values (approximately 8.6 K) within the shaded area support the existence of a line-phase superconducting phase in K_xWS_2 between $x = 0.05$ and 0.2. This is consistent with the conventional staging effect frequently observed in the intercalated states of layered systems[38]. The chemical composition x of the superconducting phase should be accurately determined by Raman spectroscopy and X-ray diffraction. When potassium is intercalated beyond the optimal range, superconductivity finally disappeared ($T_c = 0$), implying a possible phase change to the overdoped non-superconducting compound. Fig. 5b shows that the electrochemically doped WS_2 exhibited an abrupt superconducting transition at T_c. This result contrasts strikingly with the electrostatically gated $MoSe_2$, for which we observed rather broad superconducting transitions that can be interpreted as a fluctuation phenomenon of the 2D nature of superconductivity[39]. Similar feature is also observed in other electric field induced superconductivity, for instance, in $SrTiO_3$[40]. The sharp resistance drop in the K intercalated WS_2, on the other hand, indicates that this system behaves as a three-dimensional (3D) or at least anisotropic 3D superconductor.

Discussion

In this study, we report the discovery of superconductivity in 2*H*-type $MoSe_2$, $MoTe_2$ and WS_2 induced by a crossover from electrostatic to electrochemical doping as an exploratory tool to access wide and controllable doping regimes. Following the established electrostatic doping, we discovered the presence of previously unknown gate-induced superconductivity in $MoSe_2$ but failed to find it in $MoTe_2$ because of the lower efficiency of electron accumulation in the latter. By replacing the IL with a $KClO_4$/PEG electrolyte, we accessed the adjacent intermediate doping regime and further electrochemical doping regime beyond the electrostatic limit, where superconductivity was successfully discovered for $MoTe_2$ and WS_2. To the best of our knowledge, these two materials are new, unprecedented superconductors. The discovery of a superconductor series in Mo and W chalcogenides proves that superconductivity is

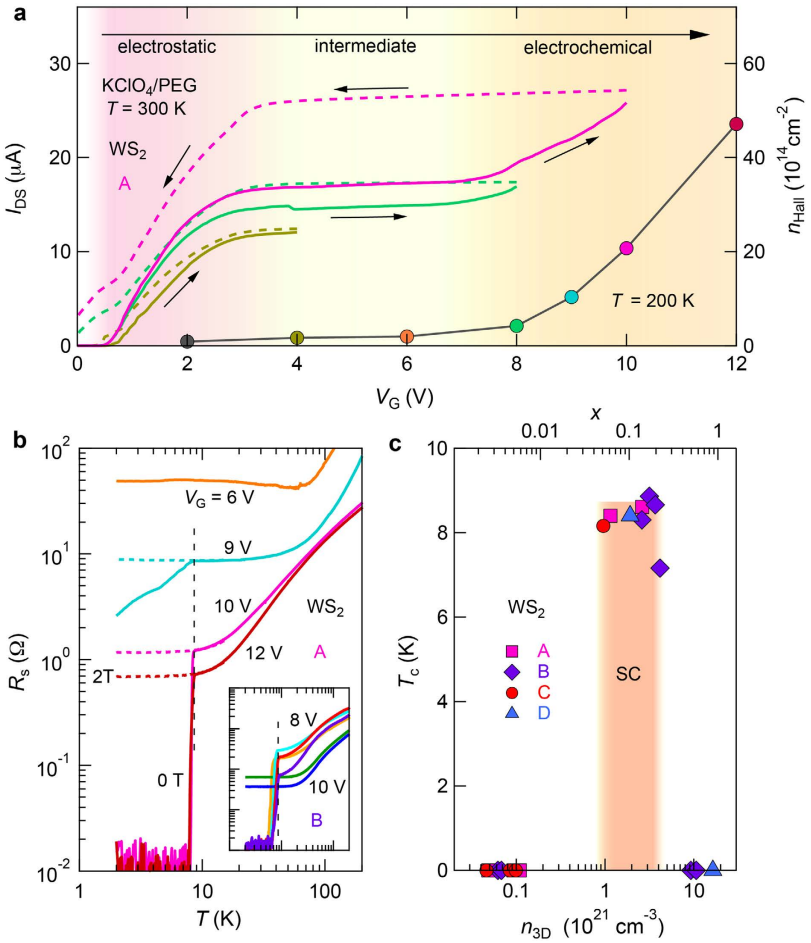

Figure 5. I_{DS}–V_G characteristics and superconductivity in WS_2 induced by electrochemical doping with $KClO_4$/PEG as ionic media. (**a**) Channel current I_{DS} (left axis) versus V_G characteristics of the WS_2 device A obtained by sweeping the $KClO_4$/PEG gate at 300 K at constant rate of 20 mV/s with $V_{DS} = 0.1$ V. The solid lines indicate the forward V_G scan of I_{DS}, followed by immediate cooling of the device for low temperature transport measurements fixed at each maximum V_G. The dashed lines were obtained via a backward scan of V_G after the device was warmed up to 300 K. Right axis shows carrier density n_{Hall} (denoted by circle symbols) plotted as a function of V_G measured at 200 K. (**b**) Temperature dependence of R_s in log scale for the same WS_2 device A at various V_G from 6 V to 12 V. The solid and dashed curves represent the data obtained for magnetic fields at 0 T and 2 T, respectively. The inset shows R_s versus T in the same log scale for another WS_2 device B at various V_G from 8 V to 10 V. The vertical dashed line indicates that the same onset T_c was observed for different V_G, implying the existence of a line-phase K_xWS_2 compound. (**c**) Phase diagram of electron-doped WS_2 as a function of bulk carrier density n_{3D} (bottom horizontal axis) and doping concentration x (upper horizontal axis). The superconducting transition temperature T_c is defined as the position corresponding to 90% of the total resistance drop. n_{3D} and x is calculated from Hall effect and the thickness of the flake by assuming that the whole thin flake is uniformly doped. Different filled symbols represent different devices and the shaded area defines a complete superconducting (SC) region reaching "zero resistance".

a common property for semiconducting TMDs. Additionally, this study provides new strategies and guidelines for the ionic gating technique: optimization of the energy level alignment at the interface for electrostatic carrier accumulation and the use of polymer electrolyte and high gate bias to induce electrochemical doping beyond the electrostatic limit. Combination of these two doping regimes can significantly broaden the applicability of ionic gating, making it a versatile tool for the study of a wide variety of materials. Thus, this study improves the versatility and effectiveness of the ionic gating method, which may play an essential role, in combination with conventional chemical doping, in the discovery of new superconductors.

Methods

Crystal growth. MoS_2 single crystals were obtained commercially (SPI Supplies). $MoSe_2$ single crystals were grown via a chemical vapor transport (CVT) technique[41,42]. Initially, Mo and Se powders were sealed in a quartz tube. The mixture was transported by iodine gas for 14 days before the crystals were grown in a two-zone furnace with a horizontal temperature gradient that was established by maintaining the higher-temperature side (T_H) at 1050 °C and the lower-temperature side (T_L) at 950 °C. $MoTe_2$ and WS_2 single crystals were grown using the same method, with chlorine gas as the transporting agent and with a gradient established by maintaining T_H/T_L at 800 °C/750 °C for $MoTe_2$ and T_H/T_L at 1000 °C/700 °C for WS_2.

Device fabrication. Multilayered thin flakes of MX_2 were cleaved from the bulk, as-grown single crystals using the scotch tape method. Subsequently, the flakes were transferred to Nb-doped $SrTiO_3$ substrates covered with a 30 nm HfO_2 layer (grown via atomic layer deposition) and SiO_2 (300 nm)/Si substrates. We chose atomically flat thin flakes with thicknesses from 20 nm to 100 nm (by using an optical microscope)[5], which were then patterned into a Hall bar configuration via conventional microfabrication techniques. Then, electrodes were prepared by evaporating layers of 5 nm Ti/60 nm Au. A rectangular channel area was defined using a 100 nm SiO_2 negative mask or a thick electron beam resist (approximately 400 nm ZEP 520A) layer[5,19,23]. The ionic medium, i.e., the ionic liquid N,N-diethyl-N-methyl-N-(2-methoxyethyl) ammonium bis(trifluoromethanesulfonyl) imide (DEME-TFSI) or the $KClO_4$/PEG polymer electrolyte, was applied to the top of the thin flake and the side gate electrode for ionic gating. The device configuration is illustrated in Fig. 1b. The polymer electrolyte was prepared by dissolving $KClO_4$ in polyethylene glycol (PEG; $M_w = 600$) with a [K]:[O] ratio of 1:20. The solution was liquid at 300 K and underwent a glass transition below approximately 250 K.

Measurement details. All transport measurements were performed using a Quantum Design Physical Property Measurement System (Quantum Design, Inc.) in high-vacuum mode (10^{-5} Torr). To reduce the likelihood of chemical reactions between the IL and the thin flakes, the transfer curves were acquired using a constant source–drain bias voltage of 0.1 V at a gate-voltage sweep rate of 20 mV/s at 220 K[5,15]. The temperature dependences of the resistance data collected at various gate voltages were measured using a previously established process[19], *i.e.*, first performing ionic gating at 220 K, followed by a cooling period under the applied voltage and subsequent warming to 220 K for gating to another V_G. When the $KClO_4$/PEG electrolyte was used, V_G was applied at 300 K.

References

1. Novoselov, K. S. *et al.* Electric field effect in atomically thin carbon films. *Science* **306,** 666–669 (2004).
2. Novoselov, K. S. *et al.* Two-dimensional atomic crystals. *Proc. Natl. Acad. Sci. USA* **102,** 10451–10453 (2005).
3. Podzorov, V., Gershenson, M. E., Kloc, C., Zeis, R. & Bucher, E. High-mobility field-effect transistors based on transition metal dichalcogenides. *Appl. Phys. Lett.* **84,** 3301 (2004).
4. Radisavljevic, B. & Kis, A. Mobility engineering and a metal-insulator transition in monolayer MoS_2. *Nature Mater.* **12,** 815–820 (2013).
5. Zhang, Y., Ye, J., Matsuhashi, Y. & Iwasa, Y. Ambipolar MoS_2 thin flake transistors. *Nano Lett.* **12,** 1136–1140 (2012).
6. Radisavljevic, B., Radenovic, A., Brivio, J., Giacometti, V. & Kis, A. Single-layer MoS_2 transistors. *Nature Nanotech.* **6,** 147–150 (2011).
7. Wang, Q. H., Kalantar-Zadeh, K., Kis, A., Coleman, J. N. & Strano, M. S. Electronics and optoelectronics of two-dimensional transition metal dichalcogenides. *Nature Nanotech.* **7,** 699–712 (2012).
8. Xiao, D., Liu, G.-B., Feng, W., Xu, X. & Yao, W. Coupled spin and valley physics in monolayers of MoS_2 and other group-VI dichalcogenides. *Phys. Rev. Lett.* **108,** 196802 (2012).
9. Zeng, H., Dai, J., Yao, W., Xiao, D. & Cui, X. Valley polarization in MoS_2 monolayers by optical pumping. *Nature Nanotech.* **7,** 490–493 (2012).
10. Mak, K. F., He, K., Shan, J. & Heinz, T. F. Control of valley polarization in monolayer MoS_2 by optical helicity. *Nature Nanotech.* **7,** 494–498 (2012).
11. Cao, T. *et al.* Valley-selective circular dichroism of monolayer molybdenum disulphide. *Nat. Commun.* **3,** 887 (2012).
12. Zhang, Y. J., Oka, T., Suzuki, R., Ye, J. T. & Iwasa, Y. Electrically switchable chiral light-emitting transistor. *Science* **344,** 725–728 (2014).
13. Mak, K. F., McGill, K. L., Park, J. & McEuen, P. L. The valley Hall effect in MoS_2 transistors. *Science* **344,** 1489–1492 (2014).
14. Lopez-Sanchez, O., Lembke, D., Kayci, M., Radenovic, A. & Kis, A. Ultrasensitive photodetectors based on monolayer MoS_2. *Nature Nanotech.* **8,** 497–501 (2013).
15. Yuan, H. T. *et al.* High-density carrier accumulation in ZnO field-effect transistors gated by electric double layers of ionic liquids. *Adv. Funct. Mater.* **19,** 1046–1053 (2009).
16. Ono, S., Minder, N., Chen, Z., Facchetti, A. & Morpurgo, A. F. High-performance n-type organic field-effect transistors with ionic liquid gates. *Appl. Phys. Lett.* **97,** 143307 (2010).
17. Hong, K., Kim, S. H., Lee, K. H. & Frisbie, C. D. Printed, sub-2V ZnO electrolyte gated transistors and inverters on plastic. *Adv. Mater.* **25,** 3413–3418 (2013).
18. Ueno, K. *et al.* Electric-field-induced superconductivity in an insulator. *Nature Mater.* **7,** 855–858 (2008).
19. Ye, J. T. *et al.* Liquid-gated interface superconductivity on an atomically flat film. *Nature Mater.* **9,** 125–128 (2009).
20. Ueno, K. *et al.* Discovery of superconductivity in $KTaO_3$ by electrostatic carrier doping. *Nature Nanotech.* **6,** 408 (2011).
21. Ye, J. T. *et al.* Accessing the transport properties of graphene and its multilayers at high carrier density. *Proc. Natl. Acad. Sci. USA* **108,** 13002–13006 (2011).
22. Yuan, H. T. *et al.* Zeeman-type spin splitting controlled by an electric field. *Nature Phys.* **9,** 563–569 (2013).
23. Ye, J. T. *et al.* Superconducting dome in a gate-tuned band insulator. *Science* **338,** 1193–1196 (2012).
24. Koval, C. A. & Howard, J. N. Electron transfer at semiconductor electrode – liquid electrolyte interfaces. *Chem. Rev.* **92,** 411–433 (1992).

25. Bott, A. W. Electrochemistry of semiconductors. *Curr. Sep*. **17,** 87–91 (1998).
26. Gratzel, M. Photoelectrochemical cells. *Nature* **414,** 338–344 (2001).
27. Bisquert, J., Cendula, P., Bertoluzzi, L. & Gimenez, S. Energy diagram of semiconductor/electrolyte junctions. *J. Phys. Chem. Lett.* **5,** 205–207 (2014).
28. Balendhran, S., *et al.* Two-dimensional molybdenum trioxide and dichalcogenides. *Adv. Funct. Mater.* **23,** 3952–3970 (2013).
29. Kumar, A. & Ahluwalia, P. K. Electronic structure of transition metal dichalcogenides monolayers 1H-MX_2 (M = Mo, W; X = S, Se, Te) from ab-initio theory: new direct band gap semiconductors. *Eur. Phys. J. B* **85,** 186 (2012).
30. Shimada, T., Ohuchi, F. S. & Parkinson, B. A. Work function and photothreshold of layered metal dichalcogenides. *Jpn. J. Appl. Phys.* **33,** 2696–2698 (1994).
31. Zhang, Y. J., Ye, J. T., Yomogida, Y., Takenobu, T. & Iwasa, Y. Formation of a stable p-n junction in a liquid-gated MoS_2 ambipolar transistor. *Nano Lett.* **13,** 3023–3028 (2013).
32. Braga, D., Gutierrez Lezama, I., Berger, H. & Morpurgo, A. F. Quantitative determination of the band gap of WS_2 with ambipolar ionic liquid-gated transistors. *Nano Lett.* **12,** 5218–5223 (2012).
33. Shimotani, H., Asanuma, H. & Iwasa, Y. Electric double layer transistor of organic semiconductor crystals in a four-probe configuration. *Jpn. J. Appl. Phys.* **46,** 3613–3617 (2007).
34. Braga, D., Ha, M., Xie, W. & Frisbie, C. D. Ultralow contact resistance in electrolyte-gated organic thin film transistors. *Appl. Phys. Lett.* **97,** 193311 (2010).
35. Rao, G. V. S., Shafer, M. W., Kawarazaki, S. & Toxen, A. M. Superconductivity in alkaline earth metal and Yb intercalated group VI layered dichalcogenides. *J. Solid State Chem.* **9,** 323–329 (1974).
36. Jo, S., Costanzo, D., Berger, H. & Morpurgo, A. F. Electrostatically induced superconductivity at the surface of WS_2. *Nano Lett.* **15,** 1197–1202 (2015).
37. Yu, Y. J. *et al.* Gate-tunable phase transitions in thin flakes of 1T-TaS_2. *Nature Nanotech*. **10,** 270–276 (2015).
38. Dresselhaus, M. S. & Dresselhaus, G. Intercalation compounds of graphite. *Adv. Phys*. **30,** 139–326 (1981).
39. Aslamazov, L. G. & Larkin, A. I. The influence of fluctuation pairing of electrons on the conductivity of normal metal. *Phys. Lett.* **26A,** 238–239 (1968).
40. Ueno, K. *et al.* Effective thickness of two-dimensional superconductivity in a tunable triangular quantum well of $SrTiO_3$. *Phys. Rev. B* **89,** 020508(R) (2014).
41. Al-Hilli, A. A. & Evans, B. L. The preparation and properties of transition metal dichalcogenides single crystals. *J. Cryst. Grow*. **15,** 93–101 (1972).
42. Fourcaudot, G., Gourmala, M. & Mercier, J. Vapor phase transport and crystal growth of molybdenum trioxide and molybdenum ditelluride. *J. Cryst. Grow*. **46,** 132–135 (1979).

Acknowledgements

We are grateful to Yuichi Kasahara and Yoichi Nii for fruitful discussions and experimental supports. We acknowledge Hongtao Yuan for sharing his experimental results before publication. We thank Yasuhiko Imai, Shigeru Kimura, Akihiko Fujiwara for technical support of synchrotron microbeam X-ray diffraction experiments in SPring-8. This research was supported by Strategic International Collaborative Research Program (SICORP-LEMSUPER), Japan Science and Technology Agency, Grant-in-Aid for Specially Promoted Research (No. 25000003) from JSPS, Japan. The synchrotron microbeam X-ray diffraction experiments were performed at the BL13XU of SPring-8 with the approval of the Japan Synchrotron Radiation Research Institute (JASRI) (Proposal No. 2013A1355).

Author Contributions

W.S., J.T.Y. and J.M. fabricated the MX_2 devices. W.S. and N.I. investigated the transistor performance of MoX_2. J.T.Y., Y.J.Z. and Y.S. performed the transport measurements of MoS_2. W.S. carried out the transport measurements and analyzed all the data of $MoSe_2$, $MoTe_2$ and WS_2. R.S. synthesized the single crystals and did the X-ray characterization on bulk samples. M.Y., J.T.Y. and Y.J.Z. performed synchrotron micro-beam X-ray diffraction on $MoSe_2$ nanoflakes. W.S., J.T.Y. and Y.I. wrote the manuscript, with inputs from all authors.

Additional Information

Supplementary information accompanies this paper at http://www.nature.com/srep

Competing financial interests: The authors declare no competing financial interests.

How to cite this article: Shi, W. *et al.* Superconductivity Series in Transition Metal Dichalcogenides by Ionic Gating. *Sci. Rep.* **5**, 12534; doi: 10.1038/srep12534 (2015).